ADVANCING EARTH AND SPACE SCIENCE

Geophysical Research Letters

RESEARCH LETTER
10.1029/2021GL095708

Mechanisms of Fast Walker Circulation Responses to CO_2 Forcing

Kezhou Lu[1], Jie He[1], Boniface Fosu[1], and Maria Rugenstein[2]

[1]School of Earth and Atmospheric Sciences, Georgia Institute of Technology, Atlanta, GA, USA, [2]Department of Atmospheric Science, Colorado State University, Fort Collins, CO, USA

Key Points:

- Climate models disagree on the fast response of the Pacific Walker circulation to CO_2
- The disagreement is determined by models' air-sea coupling strength
- Models simulating stronger air-sea coupling establish a strengthening of the Walker circulation during fast response

Supporting Information:

Supporting Information may be found in the online version of this article.

Correspondence to:

K. Lu,
kezhou.lu@eas.gatech.edu

Citation:

Lu, K., He, J., Fosu, B., & Rugenstein, M. (2021). Mechanisms of fast Walker circulation responses to CO_2 forcing. *Geophysical Research Letters*, *48*, e2021GL095708. https://doi.org/10.1029/2021GL095708

Received 23 AUG 2021
Accepted 8 NOV 2021

Author Contributions:

Conceptualization: Kezhou Lu, Jie He
Data curation: Kezhou Lu, Maria Rugenstein
Formal analysis: Kezhou Lu
Funding acquisition: Jie He
Investigation: Kezhou Lu, Jie He, Boniface Fosu
Methodology: Kezhou Lu, Jie He, Boniface Fosu
Project Administration: Kezhou Lu
Resources: Kezhou Lu, Jie He, Boniface Fosu, Maria Rugenstein
Software: Kezhou Lu
Supervision: Jie He, Boniface Fosu, Maria Rugenstein
Validation: Kezhou Lu, Jie He, Boniface Fosu, Maria Rugenstein
Visualization: Kezhou Lu
Writing – original draft: Kezhou Lu
Writing – review & editing: Kezhou Lu, Jie He, Boniface Fosu, Maria Rugenstein

Abstract

The Walker circulation (WC) responds to CO_2 forcing at both short and long timescales. In climate models, the fast response accounts for a substantial portion of the total responses, but its mechanisms, particularly those pertaining to air-sea interactions, remain unclear. We find contrasting fast WC responses in the first 2 years of abrupt CO_2 forcing, determined by the models' air-sea coupling strength in the equatorial Pacific. In models with a strong coupling, wind anomalies induced by the instantaneous land-sea thermal contrast trigger a Bjerknes feedback, leading to cooling in the equatorial Pacific and WC strengthening. The WC weakens gradually as the Bjerknes feedback wanes and the subsurface warm pool water migrates eastward as Kelvin waves. In models with a weaker coupling, the WC weakens monotonically. Our results suggest that the inter-model discrepancy in WC changes is associated with the uncertainty in the fast component.

Plain Language Summary

The Walker circulation (WC), a large-scale tropical air flow in zonal and vertical directions, is a product of the atmosphere-ocean interaction. A strong WC is associated with a more positive air-sea coupling: as the westward trade winds accumulate warm water in the western Pacific and draw up cold water in the eastern Pacific, the zonal sea surface temperature (SST) gradient and atmospheric convection above warm regions are enhanced. The zonal SST and sea level pressure gradient reinforce the trade winds. We use multiple climate models to study the response of the WC to CO_2 at different time scales. Two different WC responses are found and the difference is determined by simulated air-sea coupling strength among models. In the first class of models, a strong air-sea coupling causes a strengthening of WC right after imposed forcing—opposite to the longterm response. In the second class of models, the WC weakens from the beginning of the simulation.

1. Introduction

The response of the Walker circulation (WC) to greenhouse gas forcing has a significant effect on tropical climate and the hydrological system. Substantial research has been done on WC changes, yet it is not entirely clear whether the WC will strengthen, weaken, or remain unchanged under continued global warming. Most fully coupled general circulation models (GCMs) project a weakening of the WC under anthropogenic global warming (He & Soden, 2015; Heede et al., 2020; Held & Soden, 2006; Seager et al., 2010; Vecchi et al., 2006), which is, however, inconsistent with the observational records in the late twentieth century. Based on observations, the strength of the WC has intensified over recent decades (Chung et al., 2019; L'Heureux et al., 2013; Meng et al., 2012). The discrepancy between climate models and observations could be attributed to the following two aspects: (a) the observed cooling trend in equatorial Pacific SST due to internal variability is not well captured by most of the GCMs (e.g., L'Heureux et al., 2013; Power & Kociuba, 2011; Zhao & Allen, 2019) and/or (b) systematic model insufficiencies such as cold tongue bias (Seager et al., 2019) or errors in simulating the equatorial undercurrent (Coats & Karnauskas, 2018). In addition, despite of the fact that most GCMs predict the WC to weaken, the degree of weakening differs substantially among models (Plesca et al., 2018). Therefore, there exists a large degree of uncertainty in modeling the WC response to greenhouse gas forcing.

As a product of the tropical air-sea interaction, changes in the WC are regulated by complex feedbacks. Based on the distinct timescales of different mechanisms, the response of WC to CO_2 forcing can be divided into fast and slow components. There are two common ways to dissect the fast response from the total: (a) fixed-SST experiment where the fast component is represented by the direct response to CO_2 forcing without any changes in SST (e.g., Bony et al., 2013; Kamae & Watanabe, 2013; Samset et al., 2016) and (b) abrupt forcing experiments in a fully coupled model where the changes in the first few years of the simulation are interpreted as the fast component (e.g., Andrews et al., 2009; Chadwick et al., 2019). The first method describes how atmosphere responds to the changes of radiative forcing without the influence of SST changes, while the second one is able to address the rapid oceanic adjustment before the long-term warming. Nonetheless, studies using either approach show that the slow response is dominated by the long-term warming of SST (He & Soden, 2015; Held & Soden, 2006), while the fast response is more complicated (Andrews et al., 2009; Bony et al., 2013; Chadwick et al., 2019; He & Soden, 2015). Mechanisms controlling fast response involve direct CO_2 forcing (e.g., Andrews et al., 2010; Gregory et al., 2004) and its subsequent surface temperature changes, including the land-sea thermal contrast (e.g., Lindzen & Nigam, 1987) and the spatial pattern of SST changes (e.g., Bony et al., 2013; He & Soden, 2015). However, their relative importance, particularly how they contribute to the inter-model discrepancy in the WC changes, is not clear. Moreover, most works focus on how each forcing factor drives changes in the WC independently, but the interaction between the WC and SST especially during the fast response period is rarely investigated.

Understanding the fast WC response in the climate models is challenging yet important. Previous studies have suggested that even though the long-term tropical mean response of the WC is controlled by slow warming of SST, the changes of spatial patterns of the WC can be independent of SST warming and persist with time (Bony et al., 2013; Chadwick et al., 2014; He & Soden, 2015). Therefore, the fast response actually accounts for a substantial portion of the total response. Our study investigates the underlying mechanisms of the fast WC response with a focus on the role of fast air-sea interactions. Two opposite fast WC responses are presented in different models, each associated with a distinct transition into the slow response.

2. Methods

2.1. Model Simulations

We analyze the abrupt $4 \times CO_2$ experiment from Phase 5 of the Coupled Model Intercomparison Project (CMIP5) (Taylor et al., 2012) and a large ensemble abrupt $4 \times CO_2$ experiments of Community Earth System Model version 1 (CESM1 LE) (Rugenstein et al., 2016). In the CESM1 LE experiment, 108 ensembles of 2-year simulations and 12 ensembles with durations longer than 10 years are branched off from the same long pre-industrial control simulation at different times. The detailed experimental design is shown in Figure S1 of Supporting Information S1. We average all ensembles in CESM1 LE to eliminate internal variability. Our results are robust with fewer ensembles (Figure S2 in Supporting Information S1). Further, we use all 27 CMIP5 models that provide all necessary variables for this study.

2.2. Definition of Fast and Slow Response

We use the fully coupled abrupt $4 \times CO_2$ experimental setup to dissect the fast and slow responses. We calculate the changes in the WC by subtracting the corresponding time period from the parent pre-industrial control simulation and Δ is used to denote the difference between the abrupt $4 \times CO_2$ experiment and pre-industrial control. We define the fast response as the changes averaged over the first 2 years after imposed forcing. The total response corresponds to the changes averaged over year 91 to year 120. We choose the first 2 years as fast response because the non-monotonic WC response driven by air-sea is mostly detected during this period. However, our findings do not sensitively depend on the exact definition of the fast response time scale. As shown in Figure 1, the robust fast response signals can be detected starting from month 7. The slow response is defined as the difference between the total and the fast response. We also use changes in local surface temperature (TS) relative to the tropical mean (referred to as relative change) to highlight the inter-model discrepancy in the equatorial Pacific region. However, using relative or absolute changes of TS does not change our conclusions (compare Figure S4 with Figure S5 in Supporting Information S1).

The WC strength is calculated as the difference of the 500 hPa pressure velocity (Ω) between the Indian-West Pacific (IWP, region between 50°–150°E and 10°S–10°N) and the central-east Pacific (CEP, region between 210°–270°E and 10°S–10°N). We normalize the anomalies in the WC strength by the long-term mean of pre-industrial control values (Equation 1). The change in the WC strength is expressed as:

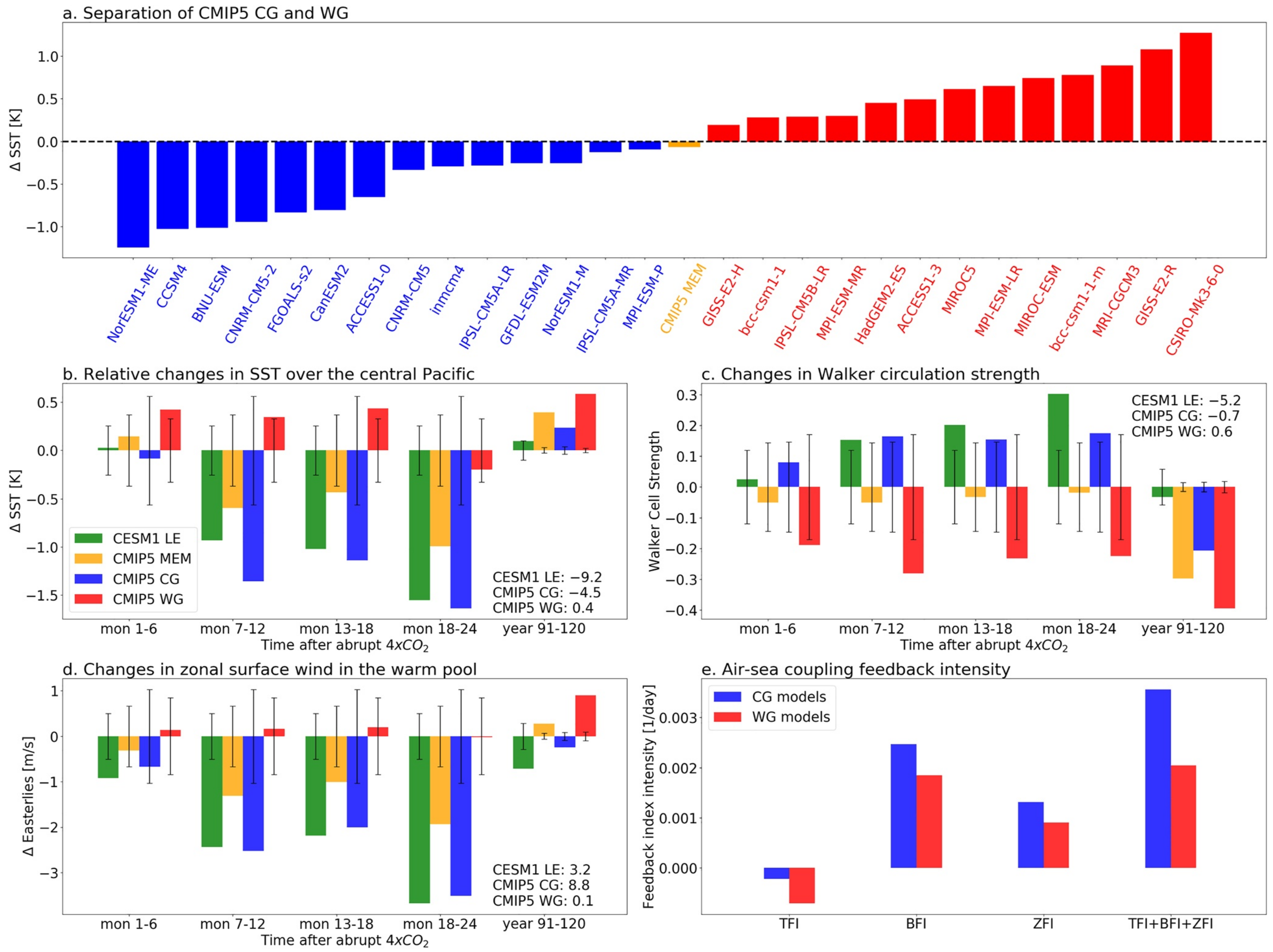

Figure 1. (a) Separation of CMIP5 CG (blue) and WG (red) groups based on the relative changes in sea surface temperature (SST) over Niño 3.4 region during fast response period. (c) Changes in the WC strength which is defined in Equation 1. (d) Changes in zonal surface wind in the Pacific warm pool (regions between 150°–180°E and 2°S–2°N). (e) Air-sea coupling feedback intensity calculated from long pre-industrial run for both CG (blue) and WG (red) (Section 2.4). CESM1 model is included as one of the CG models in (e). The orange bar in plot (a) indicates the multi-model ensemble mean. The relative changes in SST in (a and b) are calculated by subtracting mean changes in SST over the entire tropical (30°S–30°N) mean. In plot (c), positive values indicate a strengthening of Walker circulation and vice versa. The error bars in plots (b–d) indicate the range of internal variability (Section 2.3). The texts on plots (b–e) are the ratio of the fast response to the total response of different model groups.

$$\Delta WC \ \ strength = \frac{\Delta(\Omega_{500}(IWP) \ - \ \Omega_{500}(CEP))}{piControl(\Omega_{500}(IWP) \ - \ \Omega_{500}(CEP))} \tag{1}$$

2.3. Robustness

We define a response as robust if it surpasses the range of internal variability. The internal variability range is determined by the Monte Carlo method. We quantify the range of internal variability associated with changes averaged over time length (M, months or years) and ensemble members (N, corresponding to the number of CMIP5 models or the number of CESM1 ensemble members) as the following: We first calculate the difference between two non-overlapping M months or M years randomly sampled from the long pre-industrial control simulation. This is done for each ensemble/model member for a total of N times and the average difference is denoted as X. This process is repeated 5,000 times to produce a probability distribution of X. We determine robustness by using a 95% confidence level (shown as error bars in Figure 1) based on the Student's t-distribution of X.

2.4. Measuring Air-Sea Coupling Strength in the Equatorial Pacific

We measure a model's air-sea coupling strength in the equatorial Pacific based on its long pre-industrial control simulations. The complete air-sea coupling over the tropical Pacific consists of three feedbacks: the thermodynamic, Bjerknes, and zonal advection feedback. Inspired by L. Liu et al. (2011), we come up with the following framework to quantify each feedback. We first start with the mixed-layer column integrated SST tendency equation:

$$\frac{\partial T'}{\partial t} = \frac{Q'}{\rho c_p h} + \frac{\overline{w}}{h}(T_e' - T') + \frac{w'}{h}(\overline{T}_e - \overline{T}) - u'\frac{\partial \overline{T}}{\partial x} - \overline{u}\frac{\partial T'}{\partial x} - v'\frac{\partial \overline{T}}{\partial y} - \overline{v}\frac{\partial T'}{\partial y} \tag{2}$$

where T, T_e denote the temperature at the surface and at the bottom of the mixed layer respectively; Q is the net downward heat flux from the atmosphere and can be written as the sum of net downward shortwave radiation (SW), net downward longwave radiation (LW), sensible heat flux (SH) and latent heat flux(LH); ρ and C_p are the seawater density and specific heat, respectively; h is the ocean mixed layer depth; and u, v, and w are column averaged ocean current velocities in the zonal, meridional, and vertical directions, respectively. The overhead bar denotes the climatological mean and the prime denotes the anomalies calculated from July-September (JAS) mean with the annual cycle removed. By scaling analysis, the following terms: $\frac{SH'}{\rho c_p h}$, $\frac{LW'}{\rho c_p h}$, $\frac{w'}{h}(\overline{T}_e - \overline{T})$, $\overline{u}\frac{\partial T'}{\partial x}$, $v'\frac{\partial \overline{T}}{\partial y}$ and $\overline{v}\frac{\partial T'}{\partial y}$ are much smaller than the other terms (see Figure S3 in Supporting Information S1 for details). Therefore Equation 2 can be simplified as:

$$\frac{\partial T'}{\partial t} \approx \frac{1}{\rho c_p h}(SW' + LH') + \frac{\overline{w}}{h}(T_e' - T') - u'\frac{\partial \overline{T}}{\partial x} \tag{3}$$

We assume T' follows an exponential decay (or growth) during a short period of time:

$$\frac{dT'}{dt} = -\frac{\lambda}{\rho c_p h}T' \tag{4}$$

$$T' = Ae^{-\frac{\lambda}{\rho c_p h}t} \tag{5}$$

We take the time derivative of T' and plug it into Equation 3:

$$\frac{\overline{w}}{h} - \frac{\lambda}{\rho c_p h} = \frac{1}{\rho c_p h}\frac{SW' + LH'}{T'} + \frac{\overline{w}}{h}\frac{T_e'}{T'} - \frac{\partial \overline{T}}{\partial x}\frac{u'}{T'} \tag{6}$$

We decompose $\frac{T_e'}{T'}$ as follows:

$$\frac{T_e'}{T'} = \frac{T_e'}{D'}\frac{D'}{u_{850}'}\frac{u_{850}'}{T'} \tag{7}$$

where D' is the thermocline depth anomaly and u_{850}' is the 850 hpa zonal wind anomaly. Thus, Equation 6 can be expanded as:

$$\frac{\overline{w}}{h} - \frac{\lambda}{\rho c_p h} = \frac{1}{\rho c_p h}\frac{LH' + SW'}{T'} + \frac{\overline{w}}{h}\frac{T_e'}{D'}\frac{D'}{u_{850}'}\frac{u_{850}'}{T'} - \frac{\partial \overline{T}}{\partial x}\frac{u'}{T'} \tag{8}$$

The left-hand side of Equation 8 approximates the total growth (or decay) rate of SST anomaly (SSTa). The first term on the right-hand side of Equation 8 shows how strong the latent heat flux and short wave flux is connected to the SSTa, and therefore, it represents the thermodynamic feedback. The second term indicates the anomalous subsurface temperature advected by the climatological mean upwelling velocity, and therefore, it represents the Bjerknes feedback. The Bjerknes feedback can be further decomposed into three processes: coupling between the tilt of the thermocline and subsurface temperature $\left(\frac{T_e'}{D'}\right)$, coupling between the thermocline tilt and low-level zonal wind $\left(\frac{D'}{u_{850}'}\right)$, and coupling between low-level wind and surface temperature $\left(\frac{u_{850}'}{T'}\right)$. The third term on the right-hand side of Equation 8 indicates the climatological mean zonal SST gradient advected by the anomalous zonal current.

Based on Equation 8, we define the thermodynamic feedback index (TFI), the Bjerknes feedback index (BFI), and the zonal advection feedback index (ZFI) as the following:

$$TFI = \frac{1}{\rho c_p h}(R(SW, SST) + R(LH, SST)) \tag{9}$$

$$BFI = \frac{\overline{w}}{h} R(T_e, D) R(D, u_{850}) R(u_{850}, SST) \tag{10}$$

$$ZFI = (-\frac{\partial \overline{T}}{\partial x}) R(u_o, SST) \tag{11}$$

where $R(x, y)$ denotes the linear regression coefficient between two anomalous time series x' and y'. All feedback indices have the unit: $\frac{1}{[day]}$. A positive value of the feedback index represents a positive feedback and a higher magnitude of the index represents a stronger feedback intensity. The thermodynamic feedback consists of two processes: a negative convective cloud feedback, represented by $R(SW, SST)$ and a positive wind-evaporation-SST (WES) feedback, represented by $R(LH, SST)$ (R. Liu et al., 2017; Xie et al., 2010). The thermodynamic feedback is either positive or negative depending on the tug of war between these two processes. A positive Bjerknes feedback indicates that $R(T_e, D)$, $R(D, u_{850})$, and $R(u_{850}, SST)$ are all positive. Similarly, the zonal advection feedback should be positive as the equatorial undercurrent always transports warm surface water from the west to the east.

3. Results

3.1. Fast Response

In the first month following the abrupt forcing, a rapid land-sea thermal contrast develops in all models, initiating land-ward wind anomalies near the Maritime Continent (MC) and South America (Figure S6 in Supporting Information S1). After a few months, the models' wind and SST responses start to diverge and this discrepancy is maintained throughout the entire fast response period (Figures 1b–1e; Figures S5 and S6 in Supporting Information S1). As shown later, these changes are linked to the diverse fast WC responses among models. Therefore, based on the models' relative SST changes in the Niño 3.4 region averaged over the first 2 years, we can divide them into a cold group (CG) and a warm group (WG): models with values lower than the multi-model ensemble mean (CMIP5 MEM) are grouped into the CG and the rest are grouped into the WG. CESM1 LE belongs to the CG models (Figure 1a). We study model groups instead of individual models to minimize the effect of internal variability.

In the first 2 years after CO_2 quadrupling, CESM1 LE, and CMIP5 CG show a cooling in the central equatorial Pacific relative to the tropical mean (Figures 2a and 2c). The WC strengthens and anomalous easterlies form in the Pacific warm pool (regions between 150°–180°E and 2°S–2°N) (Figures 1c and 1d). The cooling of the central equatorial Pacific and the strengthening of the WC are connected via the Bjerknes feedback: Within the first month after applying the abrupt forcing, the anomalous easterlies in the warm pool region initiated by the rapid land-sea warming contrast trigger the Bjerknes feedback (Figures S6a and S6c in Supporting Information S1). As the positive Bjerknes feedback is activated, the deep convection over the MC strengthens, intensifying the anomalous easterlies to the east of the MC as a Kelvin wave response to the anomalous convective heating (Figure S7 in Supporting Information S1; e.g., Gill, 1980). The anomalous easterlies increase the zonal SST gradient in the equatorial Pacific, which in turn strengthens the wind anomalies. A similar Bjerknes feedback appears in the equatorial Indian Ocean, where the anomalous westerlies in the west-east SST dipole reinforce each other, and together further intensify the anomalous convection in the MC (Figure S7 in Supporting Information S1; e.g., Wang et al., 2016). As a result of the feedbacks between changes in the circulation and SST, the WC strengthens and is shifted westward (Figures 1c, 3a, and 3b). On the other hand, the land-sea warming contrast drives anomalous westerlies in the eastern Pacific (Figures 2a and 2c; Figure S6a in Supporting Information S1). The anomalous westerlies suppress the equatorial Pacific upwelling, warming the Pacific cold tongue (regions between 240°–270°E and 2°S–2°N). The fast SST and circulation responses differ substantially from the total responses in the CESM1 LE and the CMIP5 CG models (Figures 2a–2d), indicating a non-monotonic evolution of Indo-Pacific climate under CO_2 forcing.

10.1029/2021GL095708

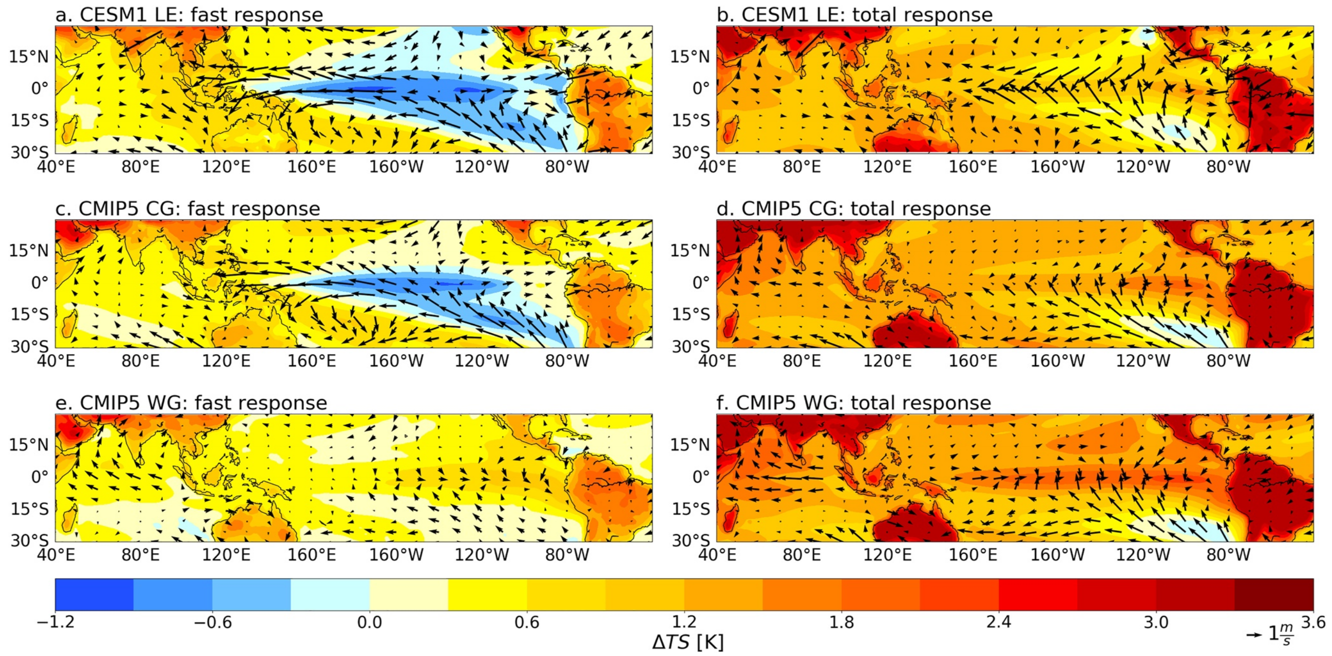

Figure 2. (a, c, and e) Fast and (b, d, and f) total response of surface temperature (shadings) and surface wind (vectors) for (a and b) CESM1 LE, (c and d) CMIP5 CG, and (e and f) CMIP5 WG. ΔTS refers to relative changes in surface temperature as detailed in Section 2.2.

The CMIP5 WG models, however, simulate a monotonic response over time. As shown in Figure 2e, enhanced warming develops in the eastern equatorial Pacific within the first 2 years, which is considerably similar to the total response (Figures 2e and 2f). The initial surface wind response includes westerly anomalies in the Pacific cold tongue driven by the warming of the South American continent but no easterly anomalies in the Pacific warm pool. The warming of the eastern equatorial Pacific in the WG models is likely driven by two mechanisms: (a) via the reduced evaporation driven by the weakening of the trade winds (i.e., a wind-evaporation-SST feedback, e.g., X. Li et al., 2016), and (b) via the weakening of the Ekman upwelling in the Pacific cold tongue region (Heede et al., 2020). It is worth mentioning that these warming mechanisms also exist in the CG models but are overpowered by the Bjerknes feedback throughout the first couple of months.

The fast response accounts for a substantial portion of the total response for both model groups. The fast response is more than four times the total response in the CG models for central Pacific SST and more than five times of total response in CESM1 LE for WC strength (texts on Figures 1b and 1c). The zonal mean pattern of WC (compare Figures 3a–3c to Figures 3g–3i) shows that the fast response pattern persists with time over the MC (around 100°–120°E) for CG models, and persists with time over the equatorial Atlantic basin (around 60°–10°W) for all both WG and CG models.

Considering the significance of the fast response, it is important to identify what causes the disparity in the fast responses between the CG models (including CESM1 LE), and the WG models. As shown in Figures 2c and 2e, the magnitude of the anomalous westerlies in the Pacific cold tongue regions are similar between the two model groups, but the CG models have much stronger anomalous easterlies in the Pacific warm pool regions, namely 2–3 m/s larger than the WG models. There is a tug of war between the anomalous easterlies in the Pacific warm pool and westerlies in the Pacific cold tongue. The anomalous easterlies dominate in the CG models, resulting in a cooling in the equatorial Pacific and a strengthening of the WC. While the anomalous westerlies act to warm the equatorial Pacific from the east, the effect is restricted to the Pacific cold tongue regions. In the WG models, however, the absence of the anomalous easterlies leads to a fast equatorial warming that is similar to the total response. The inter-model spread of the fast response can also be referred from the changes in the subsurface ocean temperature (Figures 4a–4i). In both models groups, the anomalous westerlies suppress the equatorial Pacific upwelling, warming the upper ocean in the cold

10.1029/2021GL095708

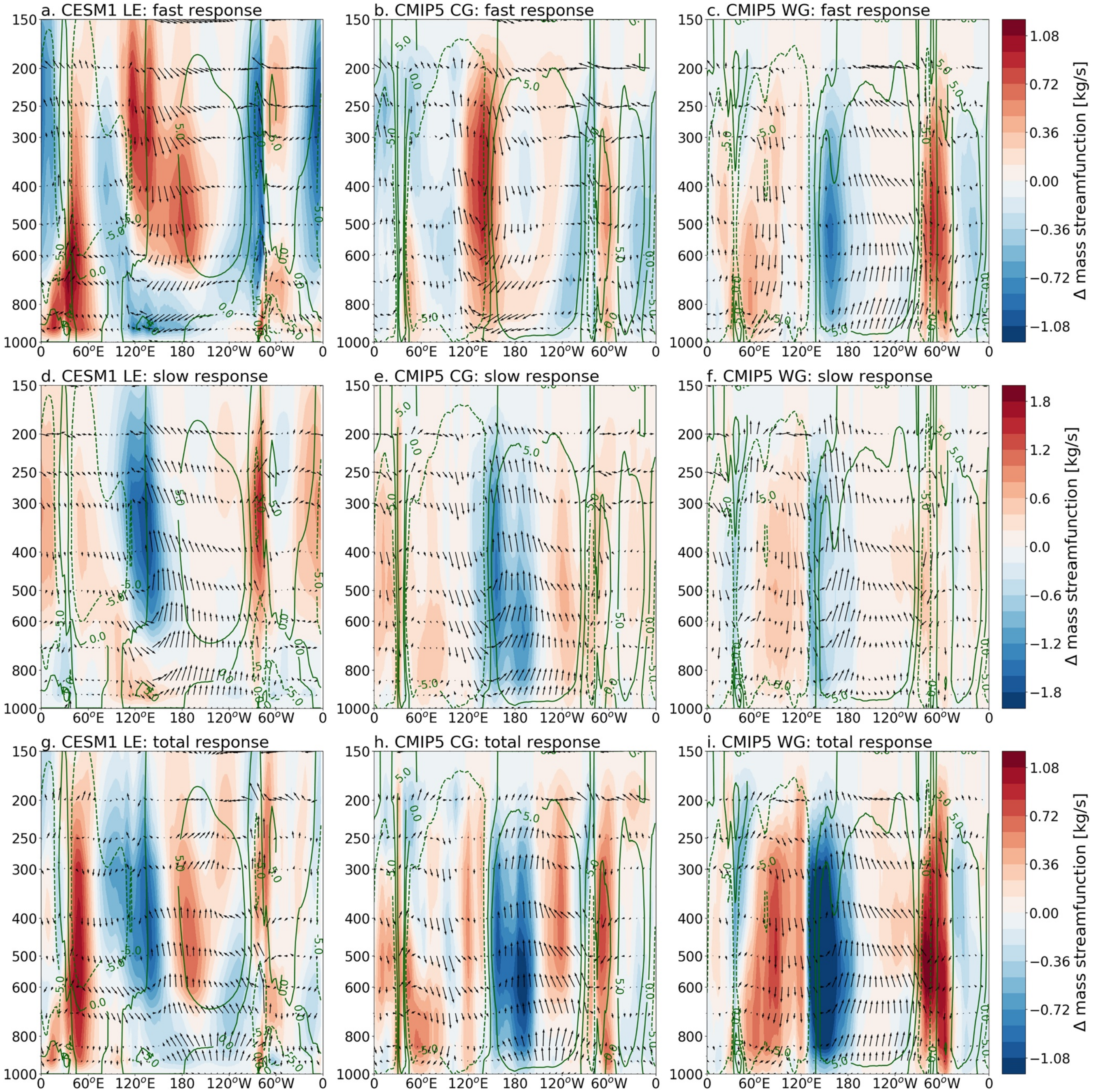

Figure 3. (a–c) The fast response, (d–f) slow response, and (g–i) total response of zonal mean mass stream functions (shadings) and vertical wind (vectors). The color bars have an interval of 0.12×10^{10} kg s^{-1} for the top and bottom rows and 0.2×10^{10} kg s^{-1} for the middle row. The vertical pressure velocity is scaled by a factor of 300. The mass stream functions are calculated with the divergent component of the zonal wind. The contours show the control climatology of the zonal mean mass stream functions with an interval of 10^{10} kg s^{-1}.

tongue region. In CG models, strong anomalous easterlies in the western Pacific deepen the thermocline, pumping cold water down below the mixed layer to the surface.

We further explore three possible mechanisms underlying the inter-model spread of the fast wind response: (a) the initial El Niño-Southern Oscillation (ENSO) state in the parent pre-industrial simulation at the time of CO_2 quadrupling could lead to a different fast wind response; (b) the surface wind and convection over the MC are more sensitive to the land-sea thermal contrast in the CG models; and (c) the CG models simulate a stronger air-sea coupling in the tropical Pacific compared to the WG models.

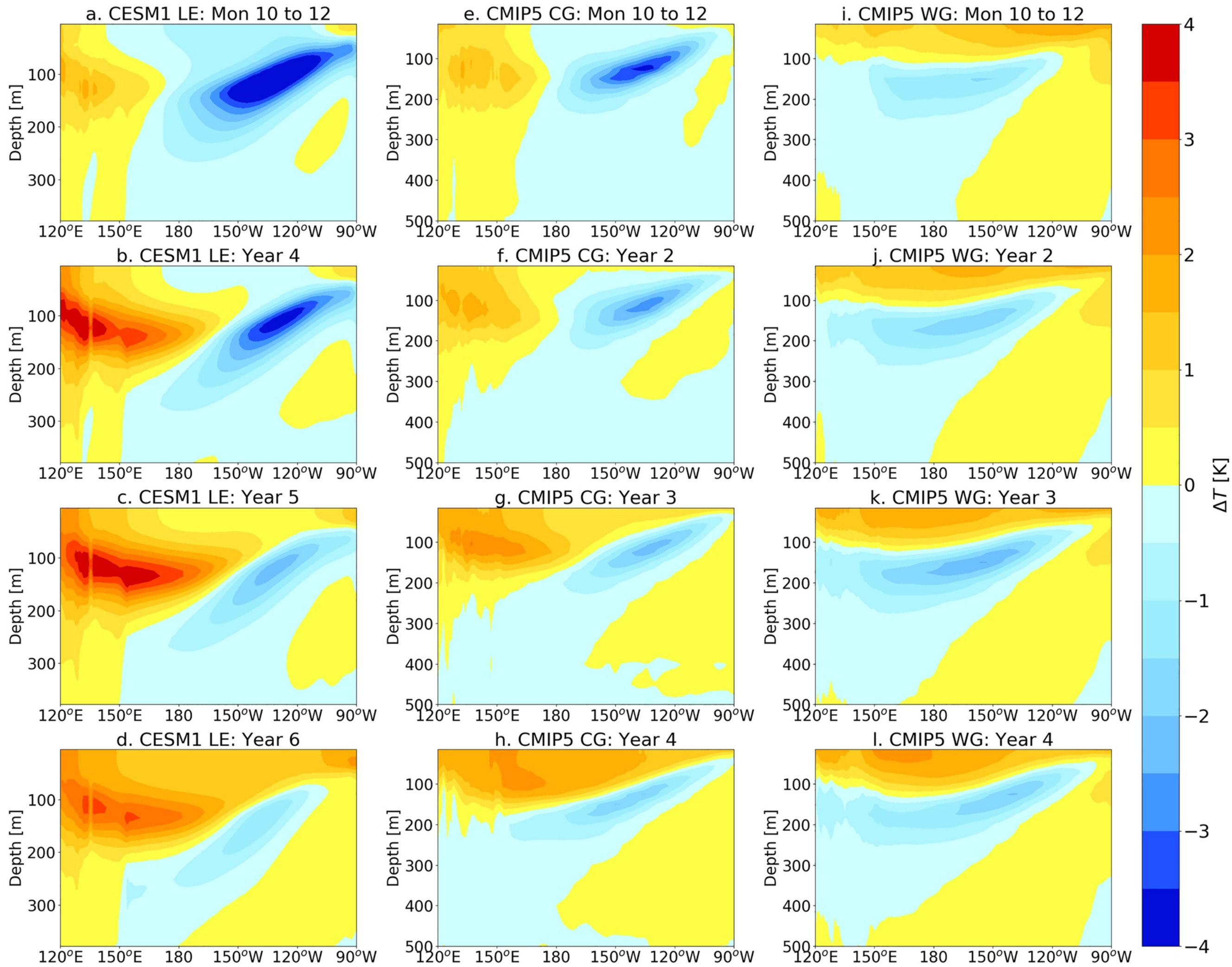

Figure 4. Time evolution of equatorial Pacific subsurface ocean temperature (averaged over 5°S–5°N) for (a, b, c, and d) CESM1 LE, (e, f, g, and h) CMIP5 CG, and (i, j, k, and l) CMIP5 WG. Years 4–6 are plotted for CESM1 LE, while Years 2–4 are plotted for CMIP5. We choose these specific time intervals to show how the downwelling Kelvin oceanic waves erase the initial Pacific cooling. The ocean temperature warms monotonically after Year 6 for all models (see Figure S20 in Supporting Information S1 for the slow response of the subsurface ocean temperature).

3.1.1. The Influence of Initial ENSO State

In CESM1 LE, 120 abrupt 4 × CO_2 simulations branch off across 120 years from a pre-industrial simulation to sample ENSO variability. Therefore, the fast strengthening of the WC in the ensemble mean is robust (the error bars in Figure 1c are much smaller than the response signals). We also investigate the ENSO state for each CMIP5 model at the time of abrupt forcing and found no remarkable influence (Figure S8 in Supporting Information S1). In addition, there is no significant relationship between parent control ENSO intensity and the first-month anomalous easterlies, which suggests that the models' fast wind response (Figure S9 in Supporting Information S1) is independent of the branch-off ENSO state. We conclude that the branch-off ENSO state is not the cause of the inter-model spread in the fast response.

3.1.2. The Influence of the Land-Sea Thermal Contrast

The relationship between the initial land-sea warming contrast and anomalous surface wind of the warm pool region reveals no significant correlation between initial land-sea warming contrast and anomalous easterlies among CMIP5 models in the first three months (Figure S10 in Supporting Information S1). In addition, in the absence of air-sea coupling, the changes in wind and the convection over the MC are similar across models as suggested from atmospheric-only simulations (Figure S11 in Supporting Information S1).

10.1029/2021GL095708

Therefore, the intensity of the land-sea thermal contrast does not contribute to the inter-model spread of the fast response.

3.1.3. Models' Air-Sea Coupling Strength

The previous analyses indicate that the air-sea coupling could cause different fast wind response. Following the method detailed in Section 2.4, we evaluated each model's air-sea coupling strength by quantifying the sign and the magnitude of the TFI, BF, and ZFI (Figures S12–S18 in Supporting Information S1) in their parent pre-industrial simulations. As shown in Figures 1e and S15 in Supporting Information S1, the CG models have a much stronger climatological ocean velocity and produce stronger WES feedback, Bjerknes feedback, and zonal feedback. In other words, the CG models simulate a stronger positive air-sea coupling compared to the WG models in the absence of any external forcing. When there is a sudden increase of CO_2 forcing, for example, abrupt $4 \times CO_2$ forcing, the land-ward wind anomalies in the Pacific warm pool induced by the initial land-sea thermal contrast can easily trigger a Bjerknes feedback in the CG models. The presence of the Bjerknes feedback intensifies the anomalous easterlies and the WC during the fast response period and thus, leads to a cooling over the central equatorial Pacific. In the WG models, on the contrary, the initial wind anomalies cannot trigger a Bjerknes feedback as the background air-sea coupling is not strong enough.

3.2. Transition From the Fast to the Slow Response

Despite the disparity in the fast response, the slow response is similar across model groups, featuring a weakening of the WC (Figures 3d–3f; He & Soden, 2015; Vecchi & Soden, 2007), and an enhanced equatorial Pacific warming (Figures 2b–2f; DiNezio et al., 2009; Heede et al., 2020; G. Li et al., 2016; Rugenstein et al., 2020; Xie et al., 2010). The amplitude of the total response is larger in the WG models because of the lack of Bjerknes feedback during the fast response period (Figures 1b and 1c). The slow response includes an anomalous upward motion over the central and eastern equatorial Pacific and an eastward shift of the WC (Figures 3d–3f). The mean SST warming and the pattern of SST warming are the two main drivers of the slow response (He & Soden, 2015). The mean SST warming weakens the convection over the Indo-west Pacific (Figures 3d–3f). This weakening can be understood from two different perspectives. From the global aspect, the global mean precipitation increases more slowly than the global mean atmospheric moisture, indicating an overall slowing down of the tropical atmospheric circulation (Vecchi & Soden, 2007). On the regional scale, the dry stability in the tropical region increases as global mean SST increases, leading to anomalous air sinking (uplifting) in the climatological ascending (descending) regions (Knutson & Manabe, 1995; Ma et al., 2012). The pattern of SST warming, particularly the enhanced equatorial Pacific warming in the eastern Pacific, contributes to the weakening of the circulation by shifting the WC eastward (He & Soden, 2015). For the WG models, much of the effect of the pattern of SST warming is achieved during the fast response (compare Figures 2e and 3c to Figure S19c in Supporting Information S1 and Figure 3f). During the slow response, the zonal SST gradient continues to weaken due to the advection of extratropical warm water, further weakening the WC over time (Heede et al., 2020; Luo et al., 2017). The sign of the total WC response is determined by the slow response for CG and WG, whereas much of the inter-model discrepancy can be attributed to the fast response.

The transition from fast to slow response for CMIP5 WG models is monotonic, as the WC continues to weaken as the mean SST increases (Figures 3c and 3f). The transition for the CESM1 LE and CMIP5 CG models starts with the weakening of convection in the MC (Figure S7 in Supporting Information S1). This could be associated with the overall weakening of tropical convection as the global mean SST increases (He & Soden, 2015) or could be caused by the diminishing effect of the land-sea warming contrast as the low-level moist static energy slowly homogenizes between the land and the ocean (Byrne & O'Gorman, 2013). As the convection weakens, so do the anomalous easterlies in the western Pacific warm pools (Figures 1d, 2b, and 2d). The Bjerknes feedback, which maintains the equatorial cooling during the fast response, starts to wane. The initial warm water anomalies that are accumulated in the warm pool by the anomalous easterlies (Figures 4a and 4e) begin to migrate eastward as downwelling Kelvin waves. Given the speed of oceanic Kelvin waves (~2–3 m/s), it takes about 4 months for the wave front to travel across the Pacific (Roundy & Kiladis, 2006). Indeed, it takes less than a year for the surface cooling to disappear, which occurs between Years 4 and 5 in the CESM1 LE (Figures 4b and 4c) and around Year 2 in the CMIP5 CG models (Figure 4f).

As the cooling pattern disappears, the CESM1 LE and the CMIP5 CG models eventually develop an enhanced equatorial warming similar to that exhibited in the WG models (Figures 4d–4i).

4. Summary and Discussions

We find two distinct fast responses of the WC to CO_2 forcing in the climate models. Whether the WC strengthens or weakens initially is determined by each model's air-sea coupling strength. In models that simulate a strong air-sea coupling, the initial land-ward wind induced by land-sea thermal contrast triggers a positive Bjerknes feedback during the fast response, leading to a strengthening and westward shift of the WC. In models that simulate a weak air-sea coupling, the central and eastern equatorial Pacific warm, leading to a fast weakening of the WC. In both model groups, the slow increase of the global mean SST eventually weakens the WC, which persists over time. We propose that the inter-model spread in simulating air-sea coupling strength contributes to the uncertainty in projecting the future changes in the WC. The timeline of the changes in the WC can be visualized in Figure S21 of Supporting Information S1.

We apply the abrupt $4 \times CO_2$ simulations to decompose the fast response from the total. In reality, however, the WC responds to changes in CO_2 simultaneously. Thus, we further explore the air-sea coupling strength in observational records and in CMIP5 historical simulations (Figure S22 in Supporting Information S1). The CG models have a stronger climatology vertical ocean velocity, a more accurate representation in the subsurface temperature-thermocline relationship, convective cloud feedback, and climatological SST gradient. The WG models do better jobs in representing the wind-SST relationship and wind-thermocline relationship. Both models have problems simulating the WES feedback, and zonal advection feedback. Overall, the CG models have a relatively more accurate air-sea coupling, but there are still large observation-model discrepancies in both models. Therefore, it is worthwhile exploring the possibility of using the observational tropical air-sea coupling strength to constrain the uncertainty in the future projection of the WC.

Data Availability Statement

The CMIP5 data can be accessed through the ESGF data portal https://esgf-node.llnl.gov/projects/cmip5/. The CESM1 pre-industrial control simulation can be obtained from https://www.cesm.ucar.edu/experiments/cesm1.1/. All the post-processing data related to this study can be downloaded via https://doi.org/10.5281/zenodo.4127653.

Acknowledgments
The authors are grateful for the resources and services provided by the Partnership for an Advanced Computing Environment (PACE) at the Georgia Institute of Technology, and the WCRP Working Group on Coupled Modeling, which is responsible for the CMIP5 multi-model ensemble. The authors thank Dr. Shoshiro Minobe and Dr. Shang-Ping Xie for the insightful discussions. The authors also thank PACE Research Scientist Fang Liu for her excellent consulting in HPC.

References

Andrews, T., Forster, P. M., Boucher, O., Bellouin, N., & Jones, A. (2010). Precipitation, radiative forcing and global temperature change. *Geophysical Research Letters*, *37*(14). https://doi.org/10.1029/2010GL043991

Andrews, T., Forster, P. M., & Gregory, J. M. (2009). A surface energy perspective on climate change. *Journal of Climate*, *22*(10), 2557–2570. https://doi.org/10.1175/2008JCLI2759.1

Bony, S., Bellon, G., Klocke, D., Sherwood, S., Fermepin, S., & Denvil, S. (2013). Robust direct effect of carbon dioxide on tropical circulation and regional precipitation. *Nature Geoscience*, *6*(6), 447–451. https://doi.org/10.1038/ngeo1799

Byrne, M. P., & O'Gorman, P. A. (2013). Link between land-ocean warming contrast and surface relative humidities in simulations with coupled climate models. *Geophysical Research Letters*, *40*(19), 5223–5227. https://doi.org/10.1002/grl.50971

Chadwick, R., Ackerley, D., Ogura, T., & Dommenget, D. (2019). Separating the influences of land warming, the direct CO_2 effect, the plant physiological effect, and SST warming on regional precipitation changes. *Journal of Geophysical Research: Atmospheres*, *124*(2), 624–640. https://doi.org/10.1029/2018JD029423

Chadwick, R., Good, P., Andrews, T., & Martin, G. (2014). Surface warming patterns drive tropical rainfall pattern responses to CO_2 forcing on all timescales. *Geophysical Research Letters*, *41*(2), 610–615. https://doi.org/10.1002/2013GL058504

Chung, E.-S., Timmermann, A., Soden, B. J., Ha, K.-J., Shi, L., & John, V. O. (2019). Reconciling opposing walker circulation trends in observations and model projections. *Nature Climate Change*, *9*(5), 405–412. https://doi.org/10.1038/s41558-019-0446-4

Coats, S., & Karnauskas, K. B. (2018). A role for the equatorial undercurrent in the ocean dynamical thermostat. *Journal of Climate*, *31*(16), 6245–6261. https://doi.org/10.1175/JCLI-D-17-0513.1

DiNezio, P. N., Clement, A. C., Vecchi, G. A., Soden, B. J., Kirtman, B. P., & Lee, S.-K. (2009). Climate response of the equatorial pacific to global warming. *Journal of Climate*, *22*(18), 4873–4892. https://doi.org/10.1175/2009JCLI2982.1

Gill, A. E. (1980). Some simple solutions for heat-induced tropical circulation. *Quarterly Journal of the Royal Meteorological Society*, *106*(449), 447–462. https://doi.org/10.1002/qj.49710644905

Gregory, J. M., Ingram, W. J., Palmer, M. A., Jones, G. S., Stott, P. A., Thorpe, R. B., & Williams, K. D. (2004). A new method for diagnosing radiative forcing and climate sensitivity. *Geophysical Research Letters*, *31*(3). https://doi.org/10.1029/2003GL018747

He, J., & Soden, B. J. (2015). Anthropogenic weakening of the tropical circulation: The relative roles of direct CO_2 forcing and sea surface temperature change. *Journal of Climate*, *28*(22), 8728–8742. https://doi.org/10.1175/JCLI-D-15-0205.1

Heede, U. K., Fedorov, A. V., & Burls, N. J. (2020). Time scales and mechanisms for the tropical pacific response to global warming: A tug of war between the ocean thermostat and weaker walker. *Journal of Climate*, *33*(14), 6101–6118. https://doi.org/10.1175/JCLI-D-19-0690.1

Held, I. M., & Soden, B. J. (2006). Robust responses of the hydrological cycle to global warming. *Journal of Climate*, *19*(21), 5686–5699. https://doi.org/10.1175/JCLI3990.1

Kamae, Y., & Watanabe, M. (2013). Tropospheric adjustment to increasing CO_2: Its timescale and the role of land–sea contrast. *Climate Dynamics*, *41*(11), 3007–3024. https://doi.org/10.1007/s00382-012-1555-1

Knutson, T. R., & Manabe, S. (1995). Time-mean response over the tropical pacific to increased CO_2 in a coupled ocean-atmosphere model. *Journal of Climate*, *8*(9), 2181–2199. https://doi.org/10.1175/1520-0442(1995)008<2181:tmrott>2.0.co;2

L'Heureux, M. L., Lee, S., & Lyon, B. (2013). Recent multidecadal strengthening of the walker circulation across the tropical pacific. *Nature Climate Change*, *3*(6), 571–576. https://doi.org/10.1038/nclimate1840

Li, G., Xie, S.-P., Du, Y., & Luo, Y. (2016). Effects of excessive equatorial cold tongue bias on the projections of tropical pacific climate change. Part I: The warming pattern in CMIP5 multi-model ensemble. *Climate Dynamics*, *47*(12), 3817–3831. https://doi.org/10.1007/s00382-016-3043-5

Li, X., Xie, S.-P., Gille, S. T., & Yoo, C. (2016). Atlantic-induced pan-tropical climate change over the past three decades. *Nature Climate Change*, *6*(3), 275–279. https://doi.org/10.1038/nclimate2840

Lindzen, R. S., & Nigam, S. (1987). On the role of sea surface temperature gradients in forcing low-level winds and convergence in the tropics. *Journal of the Atmospheric Sciences*, *44*(17), 2418–2436. https://doi.org/10.1175/1520-0469(1987)044<2418:otross>2.0.co;2

Liu, L., Yu, W., & Li, T. (2011). Dynamic and thermodynamic air-sea coupling associated with the Indian Ocean dipole diagnosed from 23 WCRP CMIP3 models. *Journal of Climate*, *24*(18), 4941–4958. https://doi.org/10.1175/2011JCLI4041.1

Liu, R., Liou, K.-N., Su, H., Gu, Y., Zhao, B., Jiang, J. H., & Liu, S. C. (2017). High cloud variations with surface temperature from 2002 to 2015: Contributions to atmospheric radiative cooling rate and precipitation changes. *Journal of Geophysical Research: Atmospheres*, *122*(10), 5457–5471. https://doi.org/10.1002/2016JD026303

Luo, Y., Lu, J., Liu, F., & Garuba, O. (2017). The role of ocean dynamical thermostat in delaying the El Niño-like response over the equatorial pacific to climate warming. *Journal of Climate*, *30*(8), 2811–2827. https://doi.org/10.1175/JCLI-D-16-0454.1

Ma, J., Xie, S.-P., & Kosaka, Y. (2012). Mechanisms for tropical tropospheric circulation change in response to global warming. *Journal of Climate*, *25*(8), 2979–2994. https://doi.org/10.1175/JCLI-D-11-00048.1

Meng, Q., Latif, M., Park, W., Keenlyside, N. S., Semenov, V. A., & Martin, T. (2012). Twentieth century walker circulation change: Data analysis and model experiments. *Climate Dynamics*, *38*(9), 1757–1773. https://doi.org/10.1007/s00382-011-1047-8

Plesca, E., Grützun, V., & Buehler, S. A. (2018). How robust is the weakening of the pacific walker circulation in CMIP5 idealized transient climate simulations? *Journal of Climate*, *31*(1), 81–97. https://doi.org/10.1175/JCLI-D-17-0151.1

Power, S. B., & Kociuba, G. (2011). The impact of global warming on the southern oscillation index. *Climate Dynamics*, *37*, 1745–1754. https://doi.org/10.1007/s00382-010-0951-7

Roundy, P. E., & Kiladis, G. N. (2006). Observed relationships between oceanic kelvin waves and atmospheric forcing. *Journal of Climate*, *19*(20), 5253–5272. https://doi.org/10.1175/JCLI3893.1

Rugenstein, M., Bloch-Johnson, J., Gregory, J., Andrews, T., Mauritsen, T., Li, C., et al. (2020). Equilibrium climate sensitivity estimated by equilibrating climate models. *Geophysical Research Letters*, *47*(4), e2019GL083898. https://doi.org/10.1029/2019GL083898

Rugenstein, M., Gregory, J. M., Schaller, N., Sedláček, J., & Knutti, R. (2016). Multiannual ocean–atmosphere adjustments to radiative forcing. *Journal of Climate*, *29*(15), 5643–5659. https://doi.org/10.1175/JCLI-D-16-0312.1

Samset, B. H., Myhre, G., Forster, P. M., Hodnebrog, Ø., Andrews, T., Faluvegi, G., et al. (2016). Fast and slow precipitation responses to individual climate forcers: A PDRMIP multimodel study. *Geophysical Research Letters*, *43*(6), 2782–2791. https://doi.org/10.1002/2016GL068064

Seager, R., Cane, M., Henderson, N., Lee, D.-E., Abernathey, R., & Zhang, H. (2019). Strengthening tropical pacific zonal sea surface temperature gradient consistent with rising greenhouse gases. *Nature Climate Change*, *9*(7), 517–522. https://doi.org/10.1038/s41558-019-0505-x

Seager, R., Naik, N., & Vecchi, G. A. (2010). Thermodynamic and dynamic mechanisms for large-scale changes in the hydrological cycle in response to global warming. *Journal of Climate*, *23*(17), 4651–4668. https://doi.org/10.1175/2010JCLI3655.1

Taylor, K. E., Stouffer, R. J., & Meehl, G. A. (2012). An overview of CMIP5 and the experiment design. *Bulletin of the American Meteorological Society*, *93*(4), 485–498. https://doi.org/10.1175/BAMS-D-11-00094.1

Vecchi, G. A., & Soden, B. J. (2007). Global warming and the weakening of the tropical circulation. *Journal of Climate*, *20*(17), 4316–4340. https://doi.org/10.1175/JCLI4258.1

Vecchi, G. A., Soden, B. J., Wittenberg, A. T., Held, I. M., Leetmaa, A., & Harrison, M. J. (2006). Weakening of tropical pacific atmospheric circulation due to anthropogenic forcing. *Nature*, *441*(7089), 73–76. https://doi.org/10.1038/nature04744

Wang, H., Murtugudde, R., & Kumar, A. (2016). Evolution of indian ocean dipole and its forcing mechanisms in the absence of ENSO. *Climate Dynamics*, *47*(7), 2481–2500. https://doi.org/10.1007/s00382-016-2977-y

Xie, S.-P., Deser, C., Vecchi, G. A., Ma, J., Teng, H., & Wittenberg, A. T. (2010). Global warming pattern formation: Sea surface temperature and rainfall. *Journal of Climate*, *23*(4), 966–986. https://doi.org/10.1175/2009JCLI3329.1

Zhao, X., & Allen, R. J. (2019). Strengthening of the Walker Circulation in recent decades and the role of natural sea surface temperature variability. *Environmental Research Communications*, *1*(2), 021003. https://doi.org/10.1088/2515-7620/ab0dab